Geophys. J. Int. (XX) **XX**, 1–12

The limits of ray theory when measuring shear wave splitting in the lowermost mantle with ScS waves

Andy Nowacki[1] and James Wookey[2]

[1] *School of Earth and Environment, University of Leeds, Leeds, LS2 9JT, UK. E-mail: a.nowacki@leeds.ac.uk*

[2] *School of Earth Sciences, University of Bristol, Wills Memorial Building, Bristol, BS8 1RJ, UK.*

Accepted 2016 September 21. Received 2016 September 19; in original form 2016 April 29.

SUMMARY

Observations of shear wave splitting provide unambiguous evidence of the presence of anisotropy in the Earth's lowermost mantle, a region known as D″. Much recent work has attempted to use these observations to place constraints on strain above the core–mantle boundary (CMB), as this may help map flow throughout the mantle. Previously, this interpretation has relied on the assumption that waves can be modelled as infinite-frequency rays, or that the Earth is radially symmetric. Due to computational constraints it has not been possible to test these approximations until now. We use fully three-dimensional, generally-anisotropic simulations of ScS waves at the frequencies of the observations to show that ray methods are sometimes inadequate to interpret the signals seen. We test simple, uniform models, and for a D″ layer as thin as 50 km, significant splitting may be produced, and we find that recovered fast orientations usually reflect the imposed fast orientation above the CMB. Ray theory in these cases provides useful results, though there are occasional, notable differences between forward methods. Isotropic models do not generate apparent splitting. We also test more complex models, including ones based on our current understanding of mineral plasticity and elasticity in D″. The results show that variations of anisotropy over even several hundred kilometres cause the ray-theoretical and finite-frequency calculations to differ greatly. Importantly, models with extreme mineral alignment in D″ yield splitting times not dissimilar to observations ($\delta t \leq 3$ s), suggesting that anisotropy in the lowermost mantle is probably much stronger than previously thought—potentially $\sim$10 % shear wave anisotropy or more. We show that if the base of the mantle is as complicated as we believe, future studies of lowermost mantle anisotropy will have to incorporate finite-frequency effects to fully interpret observations of shear wave splitting.

Key words: Seismic anisotropy; Dynamics of lithosphere and mantle; Mantle processes; Computational seismology; Body waves

1 INTRODUCTION

The Earth's lowest few hundred km—called D″—is known to show significant anisotropy (e.g., Panning & Romanowicz 2004; Kustowski et al. 2008), which is most likely caused by one or both of two things: the alignment of material of heterogeneous seismic velocity into bands or inclusions with a length scale below the seismic wavelength; or by the alignment of the lattices of intrinsically anisotropic mineral grains. In either case, this alignment must be coherent over a distance similar to or larger than the seismic wavelength. The creation of order at the core–mantle boundary (CMB), where temperatures are high and diffusive process should act relatively quickly to homogenise textures, strongly suggests that active deformation in the region is responsible. Hence there is much interest in determining if observations of anisotropy in D″ can be used to infer flow in D″ (e.g., reviews by Long & Becker 2010; Nowacki et al. 2011). Obstacles such as a lack of understanding of the exact mineralogy in D″, deformation mechanisms in D″ phases, and indeed the actual cause of the anisotropy, are large, but are being actively addressed.

Perhaps the most direct way of making observations of D″ anisotropy is using shear wave splitting in ScS waves, which traverse the lowermost mantle and reflect off the CMB. Such observations are potentially very powerful, because shear wave splitting is an unambiguous indicator of anisotropy, unlike some other methods which may trade anisotropy off with isotropic velocity variations (Kustowski et al. 2008; Ferreira et al. 2010). Furthermore, shear wave splitting measurements do not assume any particular symmetry to the Earth's elasticity, such as radial anisotropy, and hence may yield more information about flow directions than comparisons of the vertically- (SV) and horizontally-polarised (SH) shear arrivals. Several studies (Wookey et al. 2005; Wookey & Kendall 2008; Nowacki et al. 2010; Ford et al. 2015) have used splitting observations to examine D″ flow.

However, little attention has been paid to how to use ScS waves to accurately interpret flow in D″. Most frequently, a layer

thickness of the anisotropic region is assumed (often ∼150 to 300 km), and the wave is treated as a ray which has full sensitivity to the model structure along an infinitesimal path. These assumptions allow for relatively easy, rapid computation of the expected splitting from any given model of D″ anisotropy (the forward problem), and are attractive for these reasons. However, it is uncertain whether such assumptions are sufficiently accurate in order to subsequently invert for, or at least infer, possible mineral or inclusion alignment at the base of mantle.

Previous studies have investigated ray-theoretical approximations in similar cases. Chen & Tromp (2007) studied splitting in body waves from upper mantle anisotropy, but not the more complicated case of core reflections and D″ anisotropy. Cottaar & Romanowicz (2013) did not address comparisons between forward methods, but used finite-frequency, three-dimensional (3D) calculations (Capdeville et al. 2003) to model splitting in D″, though in S_{diff} waves. Similarly, Komatitsch et al. (2010b) also examined S_{diff}, concluding, like Maupin (1994), before, that isotropic velocity variations in D″ can lead to apparent splitting; neither case again addressed ScS waves. Kawai & Geller (2010) questioned the utility of using ScS wave splitting, using DSM modelling (Geller & Ohminato 1994; Kawai et al. 2006) of D″ radial anisotropy to argue that SV waves have no sensitivity at the frequencies used in shear wave splitting studies to structure at the very base of the mantle. Nonetheless, observations of splitting in D″ are numerous and some (e.g., Ritsema et al. 1998) strongly suggest that the anisotropy present is confined to the base of the mantle.

In order to resolve this standing question, we use a 3D, finite-frequency method to model a generally-anisotropic D″ with no simplifications imposed on the symmetry of elasticity. We compute synthetic seismograms for a number of simple cases where D″ is 150 and 300 km thick, with a simple style of anisotropy of the kind assumed in inversions for global radial anisotropy, but with arbitrary orientation. We also consider a geodynamically-derived model of D″ anisotropy designed to simulate more realistic variations. We then calculate the shear wave splitting produced in these models—alongside 'null case' isotropic models with the same average velocities—and show that D″ anisotropy is evidenced by splitting in ScS waves. For simple models, the recovered fast direction indeed reflects the structure present in the bottom of the mantle. Our results are consistent with that of Kawai & Geller (2010) because in generally anisotropic media, SV and SH waves do not exist and inferences based on that assumption do not apply.

For more complex, 'realistic' models of the Earth, the ray assumption appears to break down. This requires us to re-examine current explanations for the observations that exist.

2 METHODS

2.1 Forward methodology

2.1.1 Ray-based methods

Significant effort has been expended in the last few decades to the problem of ray tracing in complex, and sometimes anisotropic media (e.g., Červenỳ et al. 2007; Chapman 2010). However, these approaches often require careful intervention and the setting of a number of parameters to avoid problems such as amplitude singularities and ambiguities where sheet or point caustics occur (Thomson et al. 1992; Guest & Kendall 1993). Further, there are large difficulties in dealing with the triplications known to be present in D″, and in correctly reproducing wave interactions with the outer core, in particular for diffracted waves (Doornbos & Mondt 1979a,b; Doornbos 1981; Maupin 1994). It is further known that ray theory breaks down where smooth transitions between isotropic and anisotropic regions exist (Coates & Chapman 1990). Because of this, anisotropic ray tracing for the computation of synthetic shear wave splitting has not been widely employed in global seismology problems.

An alternative method to predict the 'effective' splitting parameters of multiple anisotropic layers is the approach first described by Silver & Savage (1994), where an analytical solution for an arbitrary number of uniform layers of anisotropy is used. In practice, the expressions frequently display unphysically large delay times near the directions in which the wave is polarised, requiring judgment and manual intervention to produce reliable results.

Instead, a 'mixed' approach is often used, where rays which have been constructed in a simpler (usually 1D) Earth model traverse a number of uniformly anisotropic domains (Abt & Fischer 2008; Wookey 2012). Within each domain, the local ray orientation is used to find the splitting operators, which are solutions to the Christoffel equation for the phase velocity for a given elastic tensor. They are then applied in turn to a synthetic wavelet with the desired polarisation and frequency characteristics (Abt & Fischer 2008), or the original waveform (Wookey 2012), and the overall effective splitting operators are finally measured using ordinary shear wave splitting analysis techniques on the split waveform.

This 'splitting operator propagation' method—the accumulation of splitting operators along predetermined ray paths, hereafter called the 'ray-theoretical' method—has been successful in studies of upper mantle anisotropy and at high frequencies (Abt & Fischer 2008; Wookey 2012; Hammond et al. 2014). This is despite two key assumptions: that the ray path is not altered much by the local (presumably) weak anisotropy; and that the wave has infinite frequency. Whilst it has been applied to ScS waves in D″ (Nowacki et al. 2013), it is uncertain whether these assumptions hold at the CMB.

2.1.2 Finite-frequency methodology

In order to test the common ray-based method, we wish to create synthetic seismograms for a generally-elastic (*i.e.*, triclinic) Earth with lateral variation in all 21 independent elastic constants; with additional symmetry imposed where appropriate. Furthermore, we wish to incorporate the finite-frequency nature of the waves. For this purpose, there currently exists only one forward modelling methodology: purely numerical discretised methods. In this study, we use the SPECFEM3D_GLOBE code (Tromp et al. 2008; Komatitsch et al. 2010a), which implements the spectral element method (SEM; Komatitsch & Vilotte 1998; Komatitsch & Tromp 1999) in a spherical Earth, using the 'cubed sphere' decomposition to divide the Earth into six chunks. Importantly, it permits arbitrary elastic structure in the mantle.

The SEM is much more computationally demanding than other forward methods traditionally used for seismic modelling, such as normal mode summation for 1D Earth models or ray theory in 3D. However, because we are interested in ScS waves, we can limit the size of the simulation box to reduce the computational overhead. We use two chunks (out of six which create the entire sphere) and enable absorbing boundary conditions on the sides of the chunks. Tests with all six chunks and no damping showed that the smaller simulations did not contain any spurious arrivals in the time periods and distance ranges of interest which would interfere with our results. In order to reach frequencies similar to the obser-

vations (∼0.1 Hz), we use 800 spectral elements along the sides of each chunk, leading to a model with in total 3.6×10^7 elements and 7.0×10^9 degrees of freedom. Each calculation of 30 minutes simulation time takes approximately one hour, using 5,000 CPU cores.

Finally, we modified the code to create the SEM mesh and then solve the forward simulation in one executable without writing mesh files to disk, similarly to Komatitsch et al. (2003). This speeds up computation when the number of elements is large because in these cases, creating the mesh and holding it in memory is faster on many systems than reading it on each occasion. Such an approach is also useful when the model is varied on each occasion, as in this study, since there is no need to write the mesh files to disk at all.

The method has been benchmarked by Komatitsch et al. (2010b) to the same frequencies as used in this study against the DSM, Green's function calculation via minor integration, and normal mode summation. We performed similar benchmarking by comparison with the DSM using the model shown in Figure 1 with radial anisotropy, and similarly found excellent agreement between the two techniques. The waveforms, and shear wave splitting derived therefrom, are essentially identical. Waveforms using the model presented in Figure 1 are shown in Figure 2.

2.2 Shear wave splitting measurements

Synthetic waveforms were measured for shear wave splitting using SHEBA (Wuestefeld et al. 2010), which implements the minimum-eigenvalue method (Silver & Chan 1991) to retrieve a set of splitting parameters which best linearise an arrival's particle motion. The program has been modified to take account of recent work highlighting the under-reporting of formal uncertainties in the measurement in the original formulation (Walsh et al. 2013). We used the multiple-window analysis method of Teanby et al. (2004) to ensure that splitting measurements were not unduly sensitive to analysis window selection. All measurements were manually inspected for quality, and care was taken to avoid including the small amount of 'SdS' energy (Figure 2) at the largest distances.

3 MODELS

The models we investigated were set in an isotropic 1D Earth model (ak135; Kennett et al. 1995), but where the velocity and density discontinuities of the transition zone are smoothed out significantly to suppress reflections from these interfaces which would otherwise interfere with the ScS arrival. We are not interested in absolute travel times, and this should have no noticeable effect on the shear wave splitting in our synthetics.

We also do not include the effects of the crust in our simulations, opting not to use a crustal model. Most studies of shear wave splitting in D″ correct for the upper mantle and crust (Nowacki et al. 2011), so we remove it entirely from our synthetic models to simplify the calculations and remove any unwanted near-receiver effects. (We note further that these corrections are often made using ray theory and might be subject to a different set of uncertainties to those discussed in this study, though this is beyond the scope of this work.) Furthermore, underside surface conversions PS and SP are much larger in most synthetics than in reality (perhaps reflecting large near-surface velocity variations and topographic effects which are not usually included), and so we make the uppermost 200 km of the mantle highly attenuating ($Q_\mu = 75$). This helps reduce SP and PS amplitudes, which in some ranges interfere with the ScS arrival.

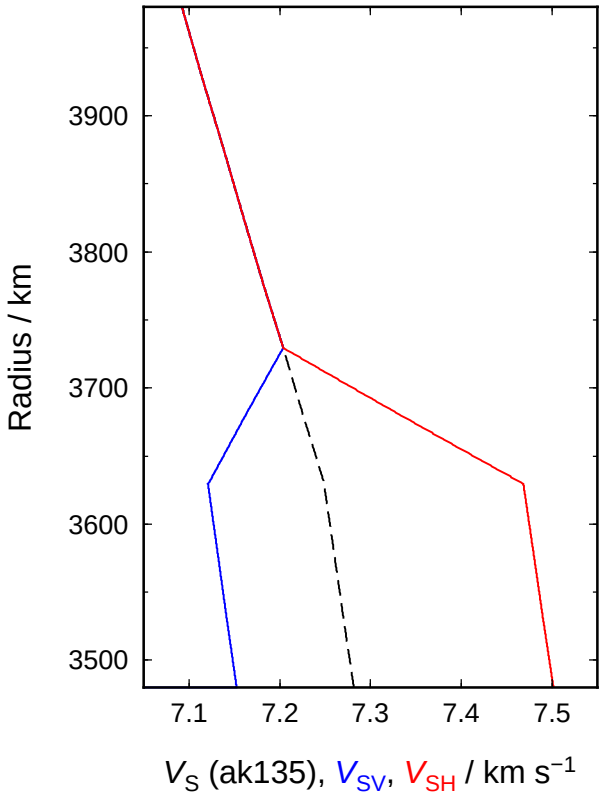

Figure 1. Velocity profile used for benchmark simulations, and in different orientations throughout this paper. V_S at the base of the mantle for the isotropic ak135 (dashed black line) and the tested model are shown. For the latter, V_{SV} is in blue and V_{SH} is in red. For the forward models investigated in section 3 onwards, the SV and SH are in a different frame, but the values are the same.

In the first two cases, we use the same type of anisotropy as shown in Figure 1, but permit it to take an arbitrary orientation. This type of anisotropy is often known as transverse isotropy (TI), where the plane normal to the axis of rotational symmetry is the plane of isotropy in which the maximum shear wave splitting occurs. It is natural then to define the elastic tensor's orientation in terms of the dip angle and dip direction of this plane. As described in Figure 3a, we vary the dip direction, d, measured clockwise from the local source–receiver direction, and the dip, γ.

3.1 Global layer of TI

We consider first a global, uniform D″ layer with constant anisotropy in the local frame (Figure 3a,b), of height h km and with a distance s over which the elastic constants vary between anisotropic and the 1D model. This is done by mixing the anisotropic constants and those representing the isotropic case using Voigt–Reuss–Hill averaging ('Hill averaging', Hill 1952) in proportion to the radial distance in the smoothing region. This requires first creating a weighted elementwise average of the two stiffness tensors for the anisotropic and isotropic velocities at a given depth (the Voigt average), then a weighted elementwise average of the equivalent compliance tensors (the Reuss average), and computing the elementwise mean of the two resulting Voigt and Reuss average stiffness tensors.

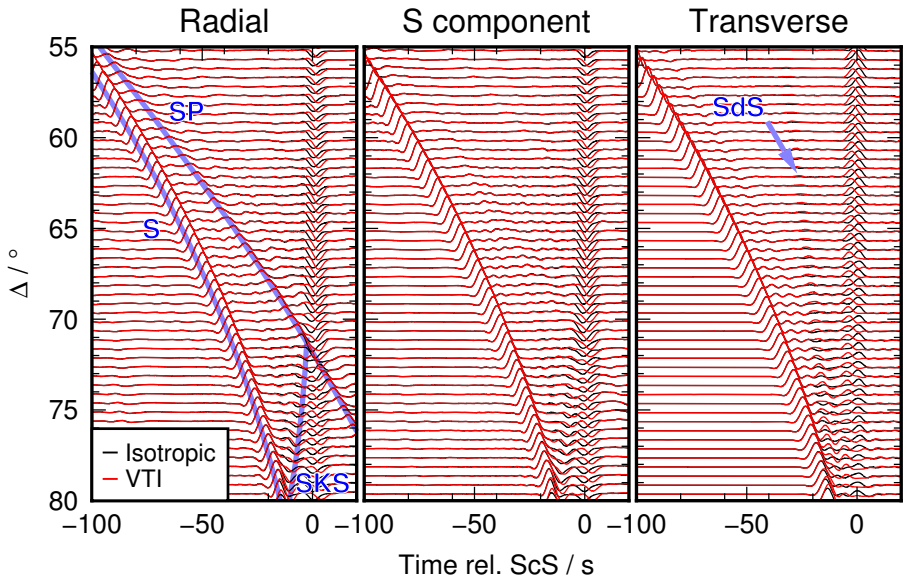

Figure 2. Comparison of S and ScS waves in synthetic seismograms from isotropic and radially-anisotropic models of D″. Black and red lines show respectively waveforms from the isotropic and anisotropic models show in Figure 1, aligned on the isotropic ScS arrival, low-pass filtered below 0.15 Hz. Radial seismograms are overlain by traveltimes for S, SP and SKS, in the ak135 model. Centre panel shows the 'S' component, correcting for the free-surface effect (Kennett 1991), and which removes the SP arrival evident in the radial seismograms. A very small reflection (SdS, shown with blue arrow) arising from the discontinuous gradient in the models is evident, arriving between S and ScS on the transverse component.

We express the anisotropy using the parameters ξ, ϕ and η (e.g., Mainprice 2007), where $\xi = V_{\mathrm{SH}}^2/V_{\mathrm{SV}}^2$, $\phi = V_{\mathrm{PV}}^2/V_{\mathrm{PH}}^2$, $\eta = c_{1133}/(V_{\mathrm{PH}}^2 - 2V_{\mathrm{SV}}^2)$, V_{SH} is the velocity of the shear wave polarised and travelling in the plane of isotropy, V_{SV} the second shear velocity when travelling in the plane of isotropy, V_{PH} the compressional velocity travelling in the plane of isotropy, and V_{PV} the compressional velocity travelling perpendicular to the plane. The 1 direction lies in the plane of isotropy and the 3 direction normal to it; c_{1133} is a linear elastic constant from the stiffness matrix c_{ijkl} for the material (Mainprice 2007).

3.2 Narrow strip of TI

We next investigate the effect of variability across the raypath (Figure 3c). We construct a model where a narrow strip of anisotropy, grading to isotropy, exists at the CMB, forming a 'tunnel' which is parallel to the projection of the ray path onto the CMB, with radius h km and smoothing distance s km. In a ray-theoretical approach, this and the previous model are identical and would not be distinguishable from only one source-receiver path.

3.3 Geodynamically-derived model

Finally, we model ScS splitting along a number of ray paths where observations exist, using a model of D″ anisotropy which best represents our current understanding of mantle dynamics. In brief, the elastic constants were created by Walker et al. (2011) using the flow field of the TX2008 model of Simmons et al. (2009) to produce strain histories at each point on a 5°-by-5° longitude-latitude grid, 100 km above the CMB. They used estimates of post-perovskite (ppv) deformation mechanisms, to perform viscoplastic self-consistent modelling along these strain histories, yielding the texture of a wholly-ppv lowermost mantle. These are combined with single-crystal elastic constants for ppv to give a generally-elastic (*i.e.*, triclinic) model of D″ which is based on a 'realistic' set of assumptions for the Earth, in the sense that the model varies spatially and in terms of anisotropy over scales of hundreds of km. Furthermore, because of uncertainties in ppv deformation mechanisms, three models were produced which yield different patterns and strengths of anisotropy, named P001, P010 and P100 to reflect the crystallographic plane along which most slip is accommodated. Hence these models provide a test of forward methodologies which might better represent the elasticity in D″ as experienced by ScS waves which are observed. The paths were previously modelled using ray methods by Nowacki et al. (2013), but for a model of ppv in D″ with multiple nodes radially as well as laterally; we use the Walker et al. (2011) constants here to minimise the spatial variability to two dimensions. These paths sample the full range of anisotropy strengths in the models, and so are a good test of the difference in the methods. Figure 4 shows the models using the Universal Elastic Anisotropy Index (A^U; Ranganathan & Ostoja-Starzewski 2008), which is measure from 0 (isotropic) upwards representing the strength of anisotropy of an arbitrary elastic tensor.

We implement these models similarly to the case of a global layer of anisotropy, as in Figure 3b, but with lateral variability in the triclinic constants. We scale the isotropic average of the constants to have the same as the background 1D model by proportionately reducing the elements of the stiffness tensor until their Hill average shear wave velocity matches the desired isotropic velocity. In doing so we enforce a smooth transition between the isotropic mantle above, and the anisotropic layer below. This is done to minimise any triplication occurring in the synthetics which may interfere with the shear wave splitting measurements. We note that many—if not most—observations of splitting in ScS have been made where the triplicated D″ discontinuity phase is not visible in the seismograms. However if we use the values of the model without scaling, a large SdS (or 'Scd') phase is visible in the finite-frequency synthetics, which is as expected because the isotropic average velocity of ppv is higher than ak135 at D″ conditions (Wookey et al. 2005). Although it is not expected to affect our splitting results, we choose

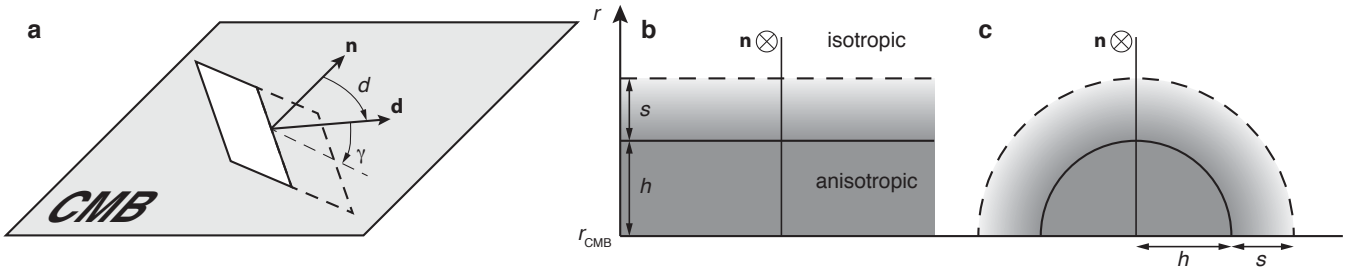

Figure 3. Models of an anisotropic D″ region. (a) Orientation of the plane of isotropy describing the TI. The dip direction, d, is measured clockwise from the local source–receiver direction, $\mathbf{n}$, in the local horizontal plane, defining the dip direction vector $\mathbf{d}$. The dip of the plane, γ, is measured downwards from the horizontal. (b) A global layer of uniform anisotropy in the local frame, and (c) a narrow strip of anisotropy in the local frame. The layer height or radius of uniform anisotropy, h, is shown, as is the smoothing distance, s. The strength of anisotropy is indicated by grey shading. The vertical black line shows the ray-theoretical path of the ScS wave, looking along $\mathbf{n}$. The radius of the CMB, r_{CMB}, is also indicated.

to minimise the SdS phase here because the triplication is not the focus of this study.

The elastic constants from Walker et al. (2011) are mapped onto the SEM mesh with the following procedure. The coordinates (radius r, longitude and latitude) of each mesh point were evaluated, and if that point was above the top of the D″ model ($r \geq r_{\mathrm{CMB}} + h + s$, where r_{CMB} is the radius of the CMB), the elastic constants representing ak135 were returned. Otherwise, the neighbouring points in the elasticity model were found, and these were used to perform bilinear interpolation between them laterally, using Voigt averaging. Points above the top of the full-strength part of the model ($r_{\mathrm{CMB}}+h < r \leq r_{\mathrm{CMB}}+h+s$) were then mixed using Hill averaging in proportion to their distance along the smoothing zone, being fully anisotropic at $r = r_{\mathrm{CMB}} + h$.

3.4 Source parameters

For the simple TI models, we use a double-couple, mainly thrust-type event with magnitude $M_W = 6$, chosen to have large shear wave amplitude along the desired direction and initially an S wave polarisation of 45°, giving similar amplitude to the SH and SV waves. It was placed at 650 km depth to minimise interference with ScS from other arrivals. Tests showed that, for all models we use in this paper, the shear wave splitting varied very little (by less than the uncertainty in the measurement) regardless of the depth of the event between 0 and 650 km. In some of the TI cases, we rotated the source to change the shear wave polarisation to observe its effect.

In the TI cases, the event was placed at a latitude of 35° south, on the Greenwich meridian (longitude of 0°) with stations placed directly north.

For the geodynamically-derived models, we used the moment tensor for the event used to make the observation from the Global-CMT project (http://www.globalcmt.org/); however, where events are shallower than 400 km, we shift them to that depth, again to minimise interference. Details are given in Table 1.

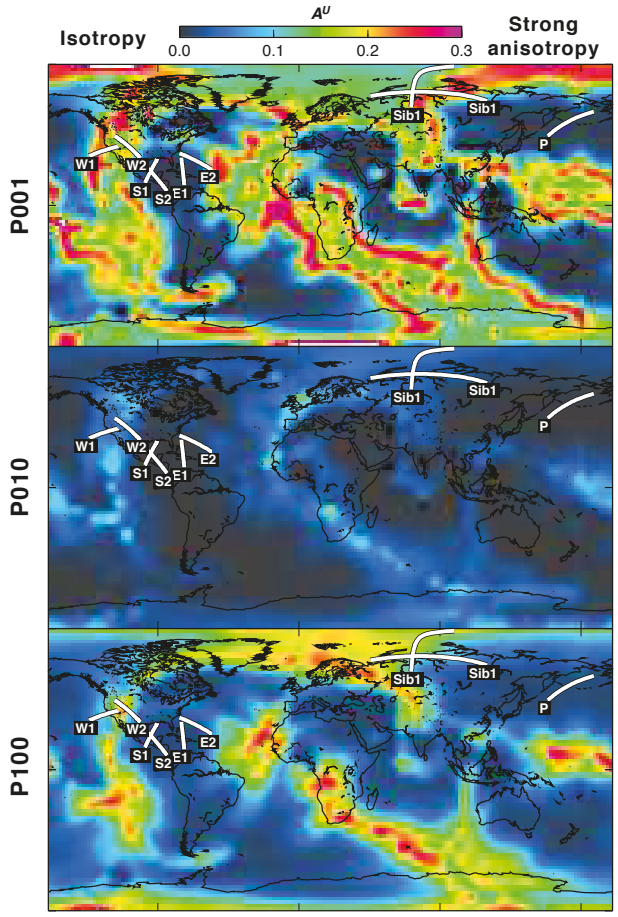

Figure 4. Geodynamically-derived models used in this study, and the paths modelled by Nowacki et al. (2013), and in this study. Thick white lines show the approximate ray path in the bottom 250 km of the mantle and are annotated with their label. Colour on plots shows the strength of the universal elastic anisotropy index, A^U (Ranganathan & Ostoja-Starzewski 2008).

4 RESULTS AND DISCUSSION

4.1 TI models

We present the shear wave splitting accrued in ScS for the TI cases. Throughout this section, we show results for epicentral distance $\Delta = 60°$, though the results are very similar for $55° \leq \Delta \leq 75°$. We show results in terms of the observed fast orientation in the ray frame (ϕ'), but also as the inferred dip. This is relevant because many previous studies (see Nowacki et al. 2011) have attempted to interpret the texture or structure in D″ in terms of the orientation of the fast shear wave, in some cases inverting for orientations (e.g., Wookey & Kendall 2008; Nowacki et al. 2010; Ford et al. 2015; Ford & Long 2015). The ray-theoretical lines and finite-frequency points should overlap in Figures 6, 7 and 10 if the ray-theoretical calculations are appropriate.

Table 1. Source parameters used in this study

Model	Path*	Source pol.† (°)	Strike (°)	Dip (°)	Rake (°)	CMTID‡
TI	-	∼45	30	40	90	-
Geodynamic	E1	113	-	-	-	C200707211327A
″	P	45	-	-	-	C070399C
″	S1	11	-	-	-	B082396C⋆
″	S2	118	-	-	-	C200707211327A
″	W1	68	-	-	-	C200708140538A⋆
″	W2◇	139	-	-	-	C200811190611A⋆

* 'TI' models have a constant path; other abbreviations are explained in Figure 4.
† Source polarisation is measured clockwise from the radial along the direction of the ScS ray.
‡ CMTID is the GlobalCMT event name, which has the format 'XMMDDYYZ' or 'XYYYYMMDDHmmZ', where YYYY and YY are four- and two-digit years, respectively, MM is the month, DD is the day, HH is the hour and mm is the minute of the event time.
⋆ Depth for these events was fixed at 400 km.
◇ The W2 source is used for the synthetic test in section 4.3.2; we do not reproduce the observations from Nowacki et al. (2013).

4.1.1 *Horizontal-ray approximation*

As an introductory aside, we first compare our ray-theoretical results to the frequently made assumption that the ScS ray is horizontal in D″ for its whole path in the anisotropic layer (Wookey et al. 2005; Wookey & Kendall 2008; Nowacki et al. 2010; Ford et al. 2015, amongst others). This approximation simplifies the interpretation of results since no epicentral distance dependence arises, and raypaths need not be calculated in an Earth model. For the simple type of anisotropy we use, the apparent along-ray dip for horizontal rays, $\gamma_{\rm app}$, is given by

$$\gamma_{\rm app} = \gamma \sin d \,. \tag{1}$$

The apparent ray-frame fast orientation, $\phi'_{\rm app}$, is measured from the vertical, so is given by

$$\phi'_{\rm app} = \gamma_{\rm app} + 90^\circ \,. \tag{2}$$

A comparison between the two predictions is shown in Figure 5. It is clear that the horizontal-ray assumption is not sufficient even for this most simple case. This is due to the fact the ray-frame fast shear wave orientation, ϕ', is not the same either side of the core reflection point, and the signal eventually accumulated reflects a combination of the splitting in each domain of anisotropy encountered. Hence, for the $d = 45^\circ$ case, the inferred dip direction is incorrect by up to 45°.

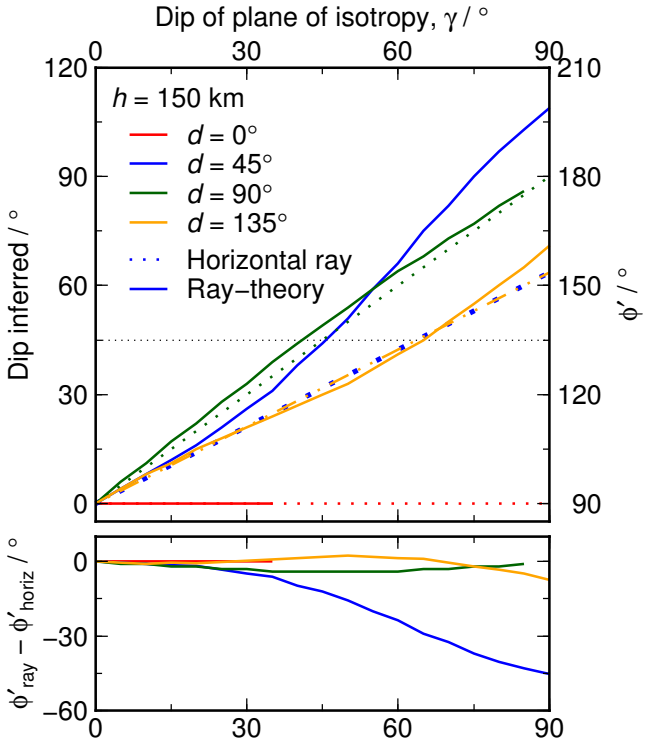

Figure 5. Shear wave splitting ray-frame fast orientation, ϕ', predicted from the global D″ layer case, where $h = 150$ km and $s = 100$ km, at $\Delta = 60^\circ$. Solid lines show the ray-theoretical results, which end when splitting becomes null. Dashed lines show ϕ' assuming the ray is horizontal in D″. Colour indicates the dip direction of the TI medium, d. Horizontal dotted black lines indicate the predicted null splitting directions, which is the same as the ray-frame incoming wave polarisation. The ray-frame fast shear wave orientation, ϕ' is shown, as well as the dip of the medium inferred, related by equation (2.)

4.1.2 *Global layer*

The ray-theoretical and finite-frequency calculations yield generally similar results, notably when d is 0°, 90° or 135°. However, the $d = 45^\circ$ case shows unintuitive results for $\gamma = 30^\circ$, 45°, where the finite-frequency and ray-theoretical splitting are wildly different. Tests varying the source polarisation and dip direction around these values show the trend is robust, and results simply from the interaction of the polarisation of the incoming wave and the elastic constants above the CMB. Modelling of anisotropic reflectivity, as done by Hall et al. (2004), does not reveal this, highlighting the unpredictable waveform effects at the CMB bounce point when the waves' true finite sensitivity is included.

The shear wave splitting delay time, δt, is not shown for the ray-theoretical calculations, but ranges from 2.0 to 6.0 s for $h = 150$ km and 3.8 to 9.5 s for $h = 300$ km. These delay times are on average about 1.5 times larger than the finite-frequency measurements. Both the magnitude and range of δt are larger for the ray-theoretical calculations. This suggests that the range of values observed in studies—up to 3 s—are representative of a thicker or stronger region of anisotropy in D″ than previously deduced using ray theory.

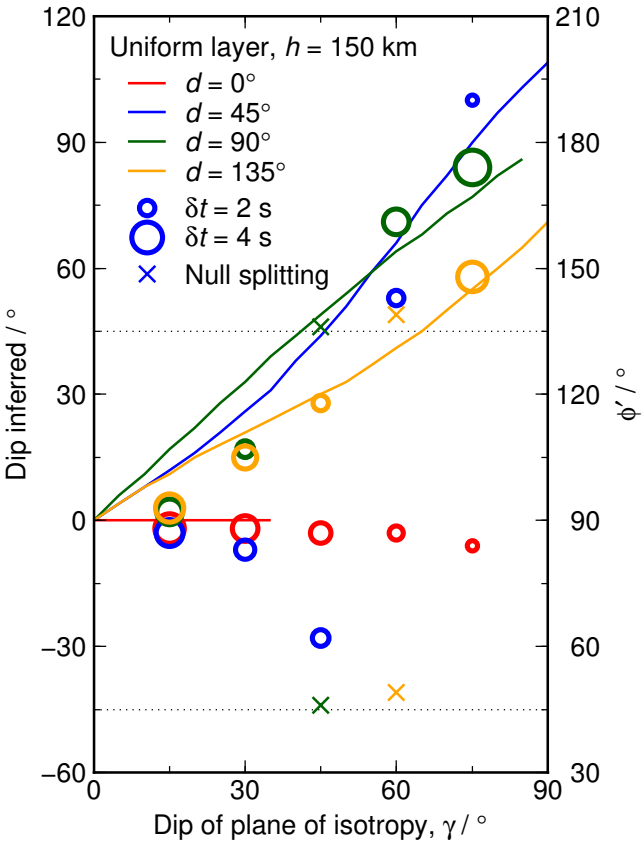

Figure 6. Shear wave splitting results from the global D″ layer case, where $h = 150$ km and $s = 100$ km, at $\Delta = 60°$. Solid lines show ray-theoretical results, which end when splitting becomes null. Circles show finite-frequency calculation results, scaled by δt, as per the legend. Where results are null, a cross is shown at the equivalent null directions. Colour indicates the dip direction of the TI medium, d. Horizontal dotted black lines indicate the predicted null splitting directions. The ray-frame fast shear wave orientation, ϕ' is shown, as well as the dip of the medium inferred. Note that finite-frequency and ray-theoretical results are generally very similar, but differ in some cases.

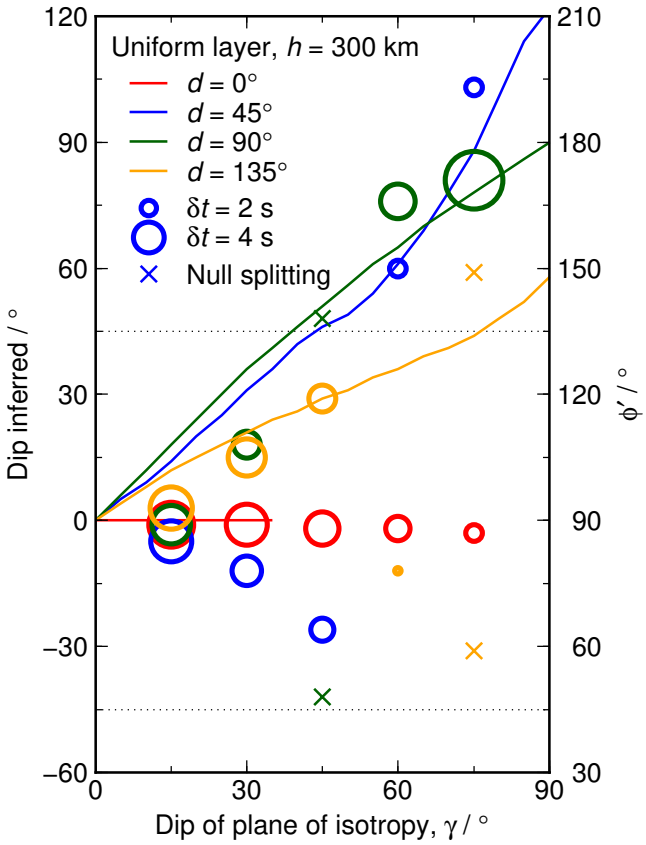

Figure 7. Shear wave splitting results from the global D″ layer case, where $h = 300$ km and $s = 100$ km. Remaining details are as for Figure 6.

4.1.3 Layer thickness and strength

To investigate the relationship between layer thickness and strength of anisotropy, we next test a number of cases where h takes a range of values between 50 and 300 km, in 50 km increments, using the same elastic parameters as in the previous section. We then test the case where the layer thickness is held at $h = 150$ km with $s = 50$ km, and vary the strength of anisotropy by changing all three anisotropic parameters equally. Figures 8 and 9 show the results for varying h and ξ, respectively.

As expected, increasing h or ξ increases δt, but it is notable that the amount of splitting does not increase monotonically with Δ, as might be expected from the style of anisotropy and the increasing path length in D″. This again highlights that even very simple cases must be treated carefully to avoid wrongly attributing variation in lowermost mantle properties when epicentral distance may be a cause. Also notable is that where $h = 0$ km, no splitting is observed. This suggests any anisotropic layer observed at the base of the mantle is likely thicker than 50 km, the smoothing distance employed in this simulation.

Maximum shear wave anisotropy in these cases is 5%, and clearly produces values of δt comparable to observations up to thicknesses of 150 km, depending on the distance range studied. The orientation chosen in this case will approximately maximise δt for a set of anisotropic parameters, placing a lower bound of the layer thickness implied here.

When varying ξ, no splitting is produced when $h = 150$ km until $\xi = 1.02$, corresponding to about 1 % maximum shear wave anisotropy. Anisotropic parameters up to 1.10 (maximum shear wave anisotropy of 5 %) are compatible with observations for most epicentral distances.

4.1.4 Narrow strip

Results for the narrow strip case are shown in Figure 10. Most results are similar to the layer case, however the $d = 0°$ case at least is different by up to 15°. For $d = 0°$, the plane of isotropy dips along the source–receiver path, and for this type of TI, ϕ' is always horizontal (90°). However, in this case, significant variation away from this results from the surrounding regions having different (isotropic) velocities to those within the strip. The effect on shear wave splitting again depends on the incoming polarisation.

It is also noteworthy that the ray-theoretical case predicts no observable splitting beyond a dip of ∼30° when $d = 90°$, for any of the models investigated so far. This effect is predictable from the form of anisotropy imposed, but the finite-frequency simulations do not show such a clear decrease in δt with γ. Hence styles and orientations of anisotropy may be represented by shear wave splitting observations in nature which appear incompatible with ray-theory calculations, when there is lateral variability in anisotropy.

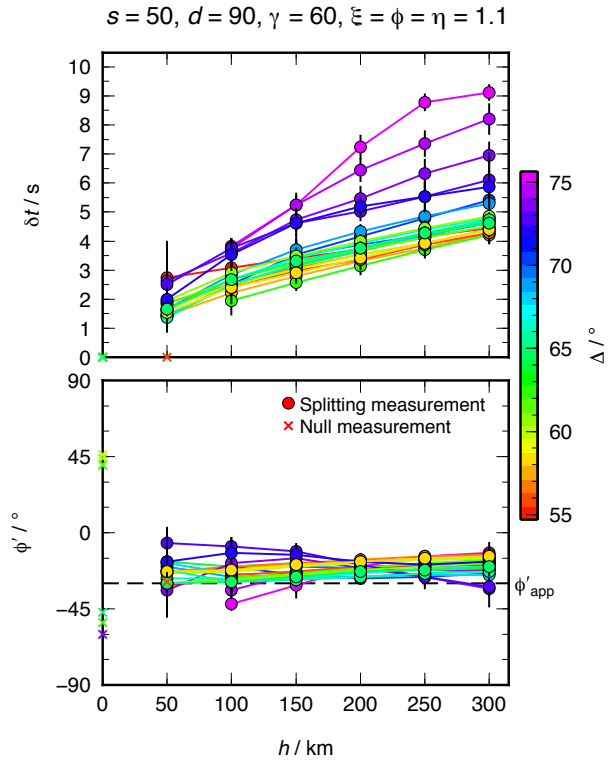

Figure 8. Shear wave splitting results from the global D′′ layer case, where the layer thickness h is varied from 0 to 300 km. Smoothing distance $s = 50$ km. The epicentral distance, Δ, is shown by colour as given in the scale. ϕ_{app} is the apparent ray-frame fast shear wave orientation assuming a horizontally-propagating ray. Coloured lines connect points with the same Δ and are broken at null or unclassifiable measurements. Error bars show formal 2σ uncertainties in the measurement.

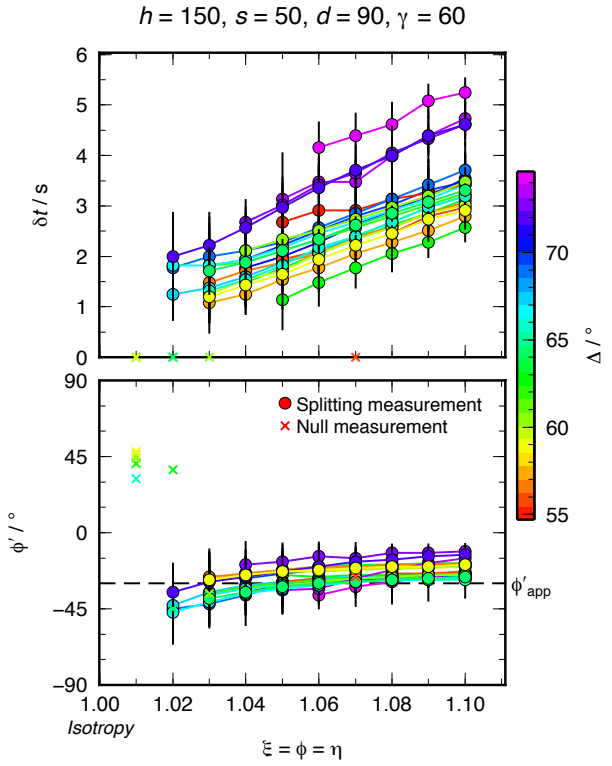

Figure 9. Shear wave splitting results from the global D′′ layer case, where the anisotropy parameters ξ, ϕ and η are varied from 1.01 to 1.10. Layer height $h = 150$ km and smoothing distance $s = 50$ km. The epicentral distance, Δ, is shown by colour as given in the scale. ϕ_{app} is the apparent ray-frame fast shear wave orientation assuming a horizontally-propagating ray. Coloured lines connect points with the same Δ and are broken at null or unclassifiable measurements.

4.2 Isotropic models

No splitting could be observed in models where no anisotropy was imposed, for any distance range in this study. Whilst other studies investigating core-diffracted waves have suggested that strong velocity variations can cause apparent splitting (Maupin 1994; Komatitsch et al. 2010b), shorter-offset ScS waves have not been investigated similarly. Because ScS is a pre-critical reflection, it is unlikely that similar effects should occur in the distance range studied here. Detailed modelling of this is outside the scope of this work, but remains to be addressed in a future study.

4.3 Geodynamic models

A limitless range of synthetic models, sources and receiver geometries could be tested for sensitivity to anisotropic structure in an effort to determine the possible styles, strengths, orientations and variability of anisotropy in D′′. However, instead we next choose to test a reasonably complicated model of D′′ anisotropy which represents a geodynamically-feasible case. This is in preference to arbitrarily increasing the complexity of synthetic cases.

4.3.1 Comparison with observations

We summarise the results for the setup described in section 3.3, compared to the ray-theoretical measurements, in Figure 11. Paths E1, P, S1 and S2 sample weak to moderate anisotropy (defined as $A^U < 0.05$, whilst W1 samples much stronger regions. Note that $A^U = 0.3$ in this model corresponds to almost perfect alignment of ppv crystals, leading to a maximum shear wave anisotropy of ∼25 % in those regions. This is expected to be far stronger than exists in reality, because at the CMB diffusion and dynamic recrystallisation are expected to operate to limit texture strength. It arises in the models because no texture-limiting condition was imposed by Walker et al. (2011). Observations and previous, ray-based modelling of D′′ also suggest that maximum shear wave anisotropy is unlikely to be as large as this.

For the paths with the weakest and most uniform anisotropy, E1, P, S1 and S2, the ray-theoretical and finite-frequency calculations are quite similar. However, in general ϕ' is not the same for the two methods, and δt is smaller for the finite-frequency method—though this δt relationship is not universally true, notably for the S2 path. This immediately implies that previous interpretations of flow direction or likely mechanisms for anisotropy in D′′ using ray methods (e.g., Wookey et al. 2005; Wookey & Kendall 2008; Long 2009; Nowacki et al. 2010; He & Long 2011; Nowacki et al. 2013; Cottaar et al. 2014; Ford et al. 2015; Ford & Long 2015) may need to be revisited, even in areas of apparently 'weak' and simple anisotropy.

When the anisotropy becomes more complex, as along S1, splitting parameters are very different. The path with the strongest and most complex elasticity, W1, shows the largest discrepancy, and very large delay times of up to $\delta t = 7$ s. The ray-theoretical calculations break down for the P010 case, as the synthetic wave-

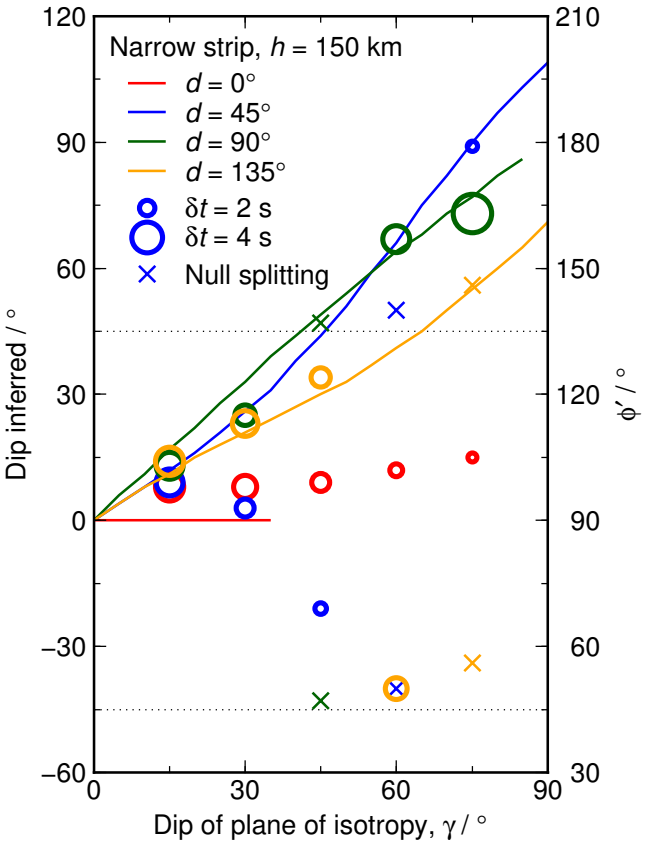

Figure 10. Shear wave splitting results from the narrow strip case, where $h = 150$ km and $s = 100$ km. Remaining details are as for Figure 6.

forms become too complicated to be adequately linearised by a single splitting operator, breaking the assumption in the minimum-eigenvalue shear wave splitting analysis method (Silver & Chan 1991). Similar problems occur for some finite-frequency calculations in tests with even stronger anisotropy, not shown here.

4.3.2 Variation of splitting parameters laterally

Finally, we show that the smooth variation of the input elasticity model results in a similarly smooth variation in splitting parameters in the finite-frequency calculations, despite the strong disagreement with ray-theoretical results. We take the source for the W2 path in Nowacki et al. (2013), and show shear wave splitting parameters retrieved from synthetic stations at $\Delta = 65^\circ$ for azimuths between 320° and 340°, representing about 500 km distance along the CMB. These waves are sensitive to the approximate area shown in Fig. 12, and sample elastic structure with maximum shear wave anisotropy of 20 %.

5 CONCLUSIONS

We compare the utility and accuracy of the infinite-frequency approximation (ray theory) in forward modelling shear wave splitting in the lowermost mantle, an important question because of the possibility that observations of this phenomenon may help constrain mantle flow in the region. Using both simple, uniform models of D″ with a range of parameters, and a suite of more physically realistic models based on mantle flow inversions and mineral physics studies, we compute the expected shear wave splitting in ScS waves, perhaps the most common seismic phase to be studied in this way.

Simple models show that shear wave splitting can be a vital tool in inferring flow in D″. In these cases, there is generally a close correspondence between the imposed orientation of the elasticity tensor and the recovered orientation of the fast shear wave. Here, ray-theoretical calculations are a useful measure of regional fabric, though there are sometimes differences between ray-theoretical and full finite-frequency methods. If D″ is simple, then it may show uniform shear wave anisotropy up to 5 % and be up to ∼300 km thick, with the two parameters trading off.

Geodynamics-based models also lead to splitting, which is often similar to observations in nature, despite very strong, variable anisotropy. However, some regions in the model lead to much greater splitting than observed due to the strong texture present in the models. Isotropic equivalent models, of course, never induce apparent shear wave splitting in the epicentral distance range of interest.

We find that ray-based methods become unreliable for interpreting ScS measurements of D″ as the strength or complexity of anisotropy there increases, to the extent that it seems very likely that previous inferences on flow in the lowermost mantle have been prejudiced by an inadequate forward method. Whilst for the simplest single-layer cases with the simplest type of anisotropy, finite-frequency calculations and traditional ones agree, there are still some configurations in which they are very different. The differences become more acute when a more physically realistic model of D″ with smooth lateral variation over hundreds of km is permitted, even though the shear wave splitting predicted from full calculations also varies correspondingly smoothly. Whilst ray theory will continue to be the basis of first order observations of lower mantle properties, we believe that future studies of D″ using perhaps the most reliable indicator of anisotropy—shear wave splitting—will have increasingly to take into account the full sensitivity of the waves being studied.

ACKNOWLEDGMENTS

We thank two anonymous reviewers whose comments helped improve the manuscript. We are grateful to Alex Song and Ana Ferreira for interesting discussions about this work, and to J.-Michael Kendall for a helpful review of the manuscript. The research leading to these results has received funding from the European Research Council under the European Union's Seventh Framework Programme (FP7/2007–2013)/ERC Grant agreement 240473 "CoMITAC". AN was supported by a Leverhulme Early Career Fellowship. Computation was performed on ARCHER, and the CoMITAC cluster Typhon. The SPECFEM3D_GLOBE software used for the finite-frequency calculations is supported by the Computational Infrastructure for Geodynamics (http://www.cig.org/). The SHEBA program is available at https://github.com/jwookey/sheba, and other codes used to process the data at https://github.com/anowacki.

REFERENCES

Abt, D. L. & Fischer, K. M., 2008. Resolving three-dimensional anisotropic structure with shear wave splitting tomography, *Geophysical Journal International*, **173**(3), 859–886, doi:10.1111/j.1365-246X.2008.03757.x.

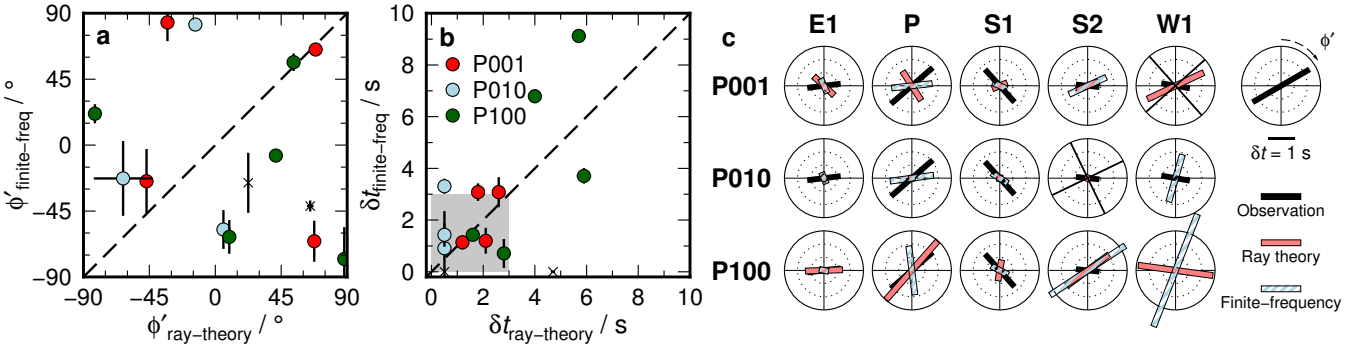

Figure 11. Summary of shear wave splitting results along five paths, using the TX2008.V2 geodynamic seismic models of Walker et al. (2011) (see text). Comparison of (a) fast orientations (ϕ') and (b) delay times (δt) between ray-theoretical calculations (subscripted 'ray-theory') and finite-frequency ('finite-freq'). Error bars show 1σ uncertainty of splitting measurement. Colour indicates the plasticity model, as per the legend in (b), whilst black crosses indicate that the finite-frequency case is null. Dashed line shows 1:1 relationship. Shaded region in (b) shows the approximate range of observed δt. (c) Comparison of synthetic splitting with observations. Black bars show the observations (same for each plasticity model). Red bars show ray-theoretical predictions, whilst light blue bars show finite-frequency calculations. Length of bar and angle indicate δt and ϕ', respectively, as shown in the key, right. Null results for the finite-frequency cases are shown with two orthogonal thin black bars along the null directions. Note that synthetic δt are usually larger and hence scaled by 0.5 so they can appear on the same plot as the data for comparison.

Capdeville, Y., To, A., & Romanowicz, B., 2003. Coupling spectral elements and modes in a spherical Earth: An extension to the 'sandwich' case, *Geophysical Journal International*, **154**(1), 44–57, doi: 10.1046/j.1365-246X.2003.01959.x.

Chapman, C. H., 2010. *Fundamentals of Seismic Wave Propagation*, Cambridge University, Cambridge.

Chen, M. & Tromp, J., 2007. Theoretical and numerical investigations of global and regional seismic wave propagation in weakly anisotropic earth models, *Geophysical Journal International*, **168**(3), 1130–1152, doi:10.1111/j.1365-246X.2006.03218.x.

Coates, R. & Chapman, C. H., 1990. Quasi-shear wave coupling in weakly anisotropic 3-D media, *Geophysical Journal International*, **103**(2), 301–320, doi:10.1111/j.1365-246X.1990.tb01773.x.

Cottaar, S. & Romanowicz, B., 2013. Observations of changing anisotropy across the southern margin of the African LLSVP, *Geophysical Journal International*, **195**(2), 1184–1195, doi:10.1093/gji/ggt285.

Cottaar, S., Li, M., McNamara, A. K., Romanowicz, B., & Wenk, H.-R., 2014. Synthetic seismic anisotropy models within a slab impinging on the core-mantle boundary, *Geophysical Journal International*, **199**(1), 164–177, doi:10.1093/gji/ggu244.

Doornbos, D. J., 1981. The effect of a second-order velocity discontinuity on elastic waves near their turning point, *Geophysical Journal International*, **64**(2), 499–511, doi:10.1111/j.1365-246X.1981.tb02679.x.

Doornbos, D. J. & Mondt, J. C., 1979a. Attenuation of P and S waves diffracted around the core, *Geophysical Journal International*, **57**(2), 353–379, doi:10.1111/j.1365-246X.1979.tb04783.x.

Doornbos, D. J. & Mondt, J. C., 1979b. P and S waves diffracted around the core and the velocity structure at the base of the mantle, *Geophysical Journal International*, **57**(2), 381–395, doi:10.1111/j.1365-246X.1979.tb04784.x.

Ferreira, A. M. G., Woodhouse, J. H., Visser, K., & Trampert, J., 2010. On the robustness of global radially anisotropic surface wave tomography, *Journal Of Geophysical Research-Solid Earth*, **115**, B04313, doi: 10.1029/2009JB006716.

Ford, H. A. & Long, M. D., 2015. A regional test of global models for flow, rheology, and seismic anisotropy at the base of the mantle, *Physics of the Earth and Planetary Interiors*, **245**, 71–75, doi: 10.1016/j.pepi.2015.05.004.

Ford, H. A., Long, M. D., He, X., & Lynner, C., 2015. Lowermost mantle flow at the eastern edge of the African Large Low Shear Velocity Province, *Earth and Planetary Science Letters*, **420**, 12–22, doi: 10.1016/j.epsl.2015.03.029.

Geller, R. J. & Ohminato, T., 1994. Computation of synthetic seismograms and their partial derivatives for heterogeneous media with arbitrary natural boundary conditions using the Direct Solution Method, *Geophysical Journal International*, **116**(2), 421–446, doi:10.1111/j.1365-246X.1994.tb01807.x.

Guest, W. S. & Kendall, J.-M., 1993. Modelling waveforms in anisotropic inhomogeneous media using ray and Maslov asymptotic theory: Applications to exploration seismology, *Canadian Journal of Exploration Geophysics*, **29**, 78–92.

Hall, S. A., Kendall, J.-M., & Van der Baan, M., 2004. Some comments on the effects of lower-mantle anisotropy on SKS and SKKS phases, *Physics of The Earth and Planetary Interiors*, **146**(3-4), 469–481, doi: 10.1016/j.pepi.2004.05.002.

Hammond, J. O. S., Kendall, J.-M., Wookey, J., Stuart, G. W., Keir, D., & Ayele, A., 2014. Differentiating flow, melt, or fossil seismic anisotropy beneath Ethiopia, *Geochemistry, Geophysics, Geosystems*, **15**(5), 1878–1894, doi:10.1002/2013GC005185.

He, X. & Long, M., 2011. Lowermost mantle anisotropy beneath the northwestern Pacific: Evidence from PcS, ScS, SKS, and SKKS phases, *Geochemistry Geophysics Geosystems*, **12**, Q12012, doi: 10.1029/2011GC003779.

Hill, R., 1952. The elastic behaviour of a crystalling aggregate, *Proc Phys Soc*, **A65**, 349–354.

Kawai, K. & Geller, R. J., 2010. The vertical flow in the lowermost mantle beneath the Pacific from inversion of seismic waveforms for anisotropic structure, *Earth and Planetary Science Letters*, **297**(1-2), 190–198, doi: 10.1016/j.epsl.2010.05.037.

Kawai, K., Takeuchi, N., & Geller, R. J., 2006. Complete synthetic seismograms up to 2 Hz for transversely isotropic spherically symmetric media, *Geophysical Journal International*, **164**(2), 411–424.

Kennett, B. L. N., 1991. The removal of free surface interactions from three-component seismograms, *Geophysical Journal International*, **104**(1), 153–163, doi:10.1111/j.1365-246X.1991.tb02501.x.

Kennett, B. L. N., Engdahl, E., & Buland, R., 1995. Constraints on seismic velocities in the Earth from travel-times, *Geophysical Journal International*, **122**(1), 108–124, doi:10.1111/j.1365-246X.1995.tb03540.x.

Komatitsch, D. & Tromp, J., 1999. Introduction to the spectral element method for three-dimensional seismic wave propagation, *Geophysical Journal International*, **139**, 806–822, doi:10.1046/j.1365-246x.1999.00967.x.

Komatitsch, D. & Vilotte, J.-P., 1998. The spectral element method: An efficient tool to simulate the seismic response of 2D and 3D geological structures, *Bulletin Of The Seismological Society Of America*, **88**(2), 368–392.

Komatitsch, D., Tsuboi, S., Ji, C., & Tromp, J., 2003. A 14.6 billion degrees of freedom, 5 teraflops, 2.5 terabyte earthquake simulation on

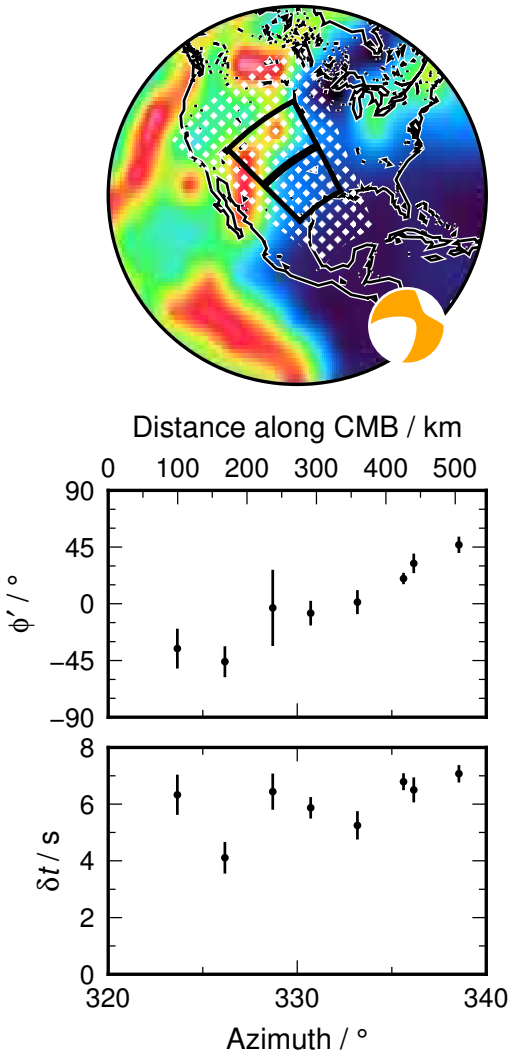

Figure 12. Shear wave splitting parameters for a number of paths at $\Delta = 65°$ from the event used in path W2. Top panel shows the approximate area of sensitivity of waves in the bottom 250 km of the mantle as stippled region: the finite-frequency sensitivity is the larger region, whilst the bounded region is the ray-theoretical area. Underlying colour shows A^U for the P001 model (scale as in Figure 4). Thick black line shows the bouncepoint of the swath. Lower hemisphere focal mechanism is shown in orange. Lower panels show ray-frame fast orientation (ϕ') and delay time (δt).

the Earth Simulator, *Proceedings of the ACM/IEEE SC2003 Conference (SC'03)*, pp. 1–8, doi:10.1145/1048935.1050155.

Komatitsch, D., Göddeke, D., Erlebacher, G., & Michéa, D., 2010a. Modeling the propagation of elastic waves using spectral elements on a cluster of 192 GPUs, *Computer Science - Research and Development*, **25**(1-2), 75–82, doi:10.1007/s00450-010-0109-1.

Komatitsch, D., Vinnik, L. P., & Chevrot, S., 2010b. SHdiff-SVdiff splitting in an isotropic Earth, *Journal Of Geophysical Research-Solid Earth*, **115**, B07312, doi:10.1029/2009JB006795.

Kustowski, B., Ekström, G., & Dziewoński, A., 2008. Anisotropic shear-wave velocity structure of the Earth's mantle: A global model, *Journal Of Geophysical Research-Solid Earth*, **113**(B6), B06306, doi:10.1029/2007JB005169.

Long, M., 2009. Complex anisotropy in D″ beneath the eastern pacific from SKS-SKKS splitting discrepancies, *Earth and Planetary Science Letters*, **283**(1-4), 181–189, doi:10.1016/j.epsl.2009.04.019.

Long, M. & Becker, T. W., 2010. Mantle dynamics and seismic anisotropy, *Earth and Planetary Science Letters*, **297**(3-4), 341–354, doi:10.1016/j.epsl.2010.06.036.

Mainprice, D., 2007. Seismic anisotropy of the deep earth from a mineral and rock physics perspective, in *Treatise on Geophysics*, vol. 2, pp. 437–492, ed. Schubert, G.

Maupin, V., 1994. On the possibility of anisotropy in the D″ layer as inferred from the polarization of diffracted S waves, *Physics of The Earth and Planetary Interiors*, **87**(1-2), 1–32, doi:10.1016/0031-9201(94)90019-1.

Nowacki, A., Wookey, J., & Kendall, J.-M., 2010. Deformation of the lowermost mantle from seismic anisotropy, *Nature*, **467**(7319), 1091–1095, doi:10.1038/nature09507.

Nowacki, A., Wookey, J., & Kendall, J.-M., 2011. New advances in using seismic anisotropy, mineral physics and geodynamics to understand deformation in the lowermost mantle, *Journal of Geodynamics*, **52**(3-4), 205–228, doi:10.1016/j.jog.2011.04.003.

Nowacki, A., Walker, A. M., Wookey, J., & Kendall, J.-M., 2013. Evaluating post-perovskite as a cause of D″ anisotropy in regions of palaeo-subduction, *Geophysical Journal International*, **192**(3), 1085–1090, doi:10.1093/gji/ggs068.

Panning, M. & Romanowicz, B., 2004. Inferences on flow at the base of Earth's mantle based on seismic anisotropy, *Science*, **303**(5656), 351–353, doi:10.1126/science.1091524.

Ranganathan, S. I. & Ostoja-Starzewski, M., 2008. Universal elastic anisotropy index, *Physical Review Letters*, **101**(5), 055504, doi:10.1103/PhysRevLett.101.055504.

Ritsema, J., Lay, T., Garnero, E. J., & Benz, H., 1998. Seismic anisotropy in the lowermost mantle beneath the Pacific, *Geophysical Research Letters*, **25**(8), 1229–1232, doi:10.1029/98GL00913.

Silver, P. G. & Chan, W. W., 1991. Shear-wave splitting and subcontinental mantle deformation, *Journal Of Geophysical Research-Solid Earth*, **96**(B10), 16429–16454, doi:10.1029/91JB00899.

Silver, P. G. & Savage, M., 1994. The interpretation of shear-wave splitting parameters in the presence of two anisotropic layers, *Geophysical Journal International*, **119**(3), 949–963, doi:10.1111/j.1365-246X.1994.tb04027.x.

Simmons, N. A., Forte, A. M., & Grand, S., 2009. Joint seismic, geodynamic and mineral physical constraints on three-dimensional mantle heterogeneity: Implications for the relative importance of thermal versus compositional heterogeneity, *Geophysical Journal International*, **177**(3), 1284–1304, doi:10.1111/j.1365-246X.2009.04133.x.

Teanby, N., Kendall, J.-M., & Van der Baan, M., 2004. Automation of shear-wave splitting measurements using cluster analysis, *Bulletin Of The Seismological Society Of America*, **94**(2), 453–463, doi:10.1785/0120030123.

Thomson, C. J., Kendall, J.-M., & Guest, W. S., 1992. Geometrical theory of shear-wave splitting: Corrections to ray theory for interference in isotropic/anisotropic transitions, *Geophysical Journal International*, **108**(1), 339–363, doi:10.1111/j.1365-246X.1992.tb00862.x.

Tromp, J., Komatitsch, D., & Liu, Q., 2008. Spectral-Element and Adjoint Methods in Seismology, *Commun Comput Phys*, **3**(1), 1–32.

Červenỳ, V., Klimeš, L., & Pšenčík, I., 2007. Seismic ray methods: recent developments, in *Advances in wave propagation in heterogeneous Earth*, no. 48 in Advances in Geophysics, pp. 1–126, eds Ru, W.-S., Maupin, V., & Dmowska, R., Elsevier.

Walker, A. M., Forte, A. M., Wookey, J., Nowacki, A., & Kendall, J.-M., 2011. Elastic anisotropy of D″ predicted from global models of mantle flow, *Geochemistry Geophysics Geosystems*, **12**(10), Q10006, doi:10.1029/2011GC003732.

Walsh, E., Arnold, R., & Savage, M. K., 2013. Silver and Chan revisited, *Journal of Geophysical Research: Solid Earth*, **118**(10), 5500–5515, doi:10.1002/jgrb.50386.

Wookey, J., 2012. Direct probabilistic inversion of shear wave data for seismic anisotropy, *Geophysical Journal International*, **189**(2), 1025–1037, doi:10.1111/j.1365-246X.2012.05405.x.

Wookey, J. & Kendall, J.-M., 2008. Constraints on lowermost mantle mineralogy and fabric beneath Siberia from seismic anisotropy, *Earth and Planetary Science Letters*, **275**(1-2), 32–42, doi:10.1016/j.epsl.2008.07.049.

Wookey, J., Kendall, J.-M., & Rümpker, G., 2005. Lowermost mantle anisotropy beneath the north Pacific from differential S–ScS splitting, *Geophysical Journal International*, **161**(3), 829–838, doi: 10.1111/j.1365-246X.2005.02623.x.

Wuestefeld, A., Al-Harrasi, O., Verdon, J. P., Wookey, J., & Kendall, J.-M., 2010. A strategy for automated analysis of passive microseismic data to image seismic anisotropy and fracture characteristics, *Geophysical Prospecting*, **58**(5), 753–771, doi:10.1111/j.1365-2478.2010.00891.x.